Supporting Information for "Love wave tomography of the United States"

Anant Hariharan[1], Colleen A. Dalton[1]

[1]Department of Earth, Environmental, and Planetary Sciences, Brown University, United States

Contents of this file

Introduction

This supporting information contains six supplementary figures, a description of the format of the phase velocity data set that is presented with this study, and a description of the processing steps used to calculate phase velocities. Text S1 describes the specific preprocessing steps used to convert travel-time measurements into Eikonal phase velocities. Figure S1 presents a comparison of four radially anisotropic models of the upper mantle beneath the U.S. Figure S2 shows, for all periods in this study, the distance-dependence of Love wave measurement error when different subsets of the full data set are isolated based on ΔT values. Figure S3 compares our phase velocity images to those from the study of (Ekström, 2017). Figure S4 presents a labeled map of physiographic features discussed in the paper. Figure S5 visualizes the uncertainties at all pixels of our phase velocity maps for all periods analyzed. Figure S6 presents global maps showing the likelihood of obtaining high-quality Love wave measurements as a function of location and period.

A zipped file containing our data set of phase velocity maps at the six periods used in this study accompanies this document.

Text S1

Our measured travel times from a single earthquake are pre-processed in several ways, broadly following the approach of Babikoff and Dalton (2019). Firstly, they are averaged in cells with longitude and latitude dimensions of $0.5° \times 0.5°$. They are then interpolated onto a gridded surface under tension, with cell size $0.25° \times 0.25°$. The surfaces are smoothed with a Gaussian filter of width 400 km. Raw measurements and pixels on this surface are only retained in the final calculation if stations exist in three non-overlapping evenly spaced azimuthal bins around the pixel or station location.

We generate phase velocities with Eikonal tomography (Lin et al., 2009). To calculate the gradient of travel time, we use a finite-difference method in spherical coordinates. This gradient is taken separately for each event, and an individual phase-velocity map for each event is solved for from the inverse of $\sqrt{|\nabla\tau|^2}$. As an outlier-removal step, individal phase-velocity measurements that differ by more than 1 km/s from the value predicted at that location from the GDM52 dispersion model (Ekström, 2011) are removed. To construct a final map at any period from all the individual event-based phase velocity maps, we take the median of all the phase-velocity measurements at any pixel. After this, pixels at the edge of the study area are removed. The map is then smoothed using a smoothing length equal to half the wavelength at the period of interest.

Data Set S1. The accompanying .zip file contains six files, each of which contains a phase velocity map for a different period considered in this study. The file naming convention is *Love_phvel_period*, where the variable *period* spans the values $35, 40, 45, 50, 60,$ or 75 s. Each file contains three columns. The first column is longitude, the second is latitude, and the third column is phase velocity at the pixel defined by the corresponding latitude/longitude pair.

Figure S1

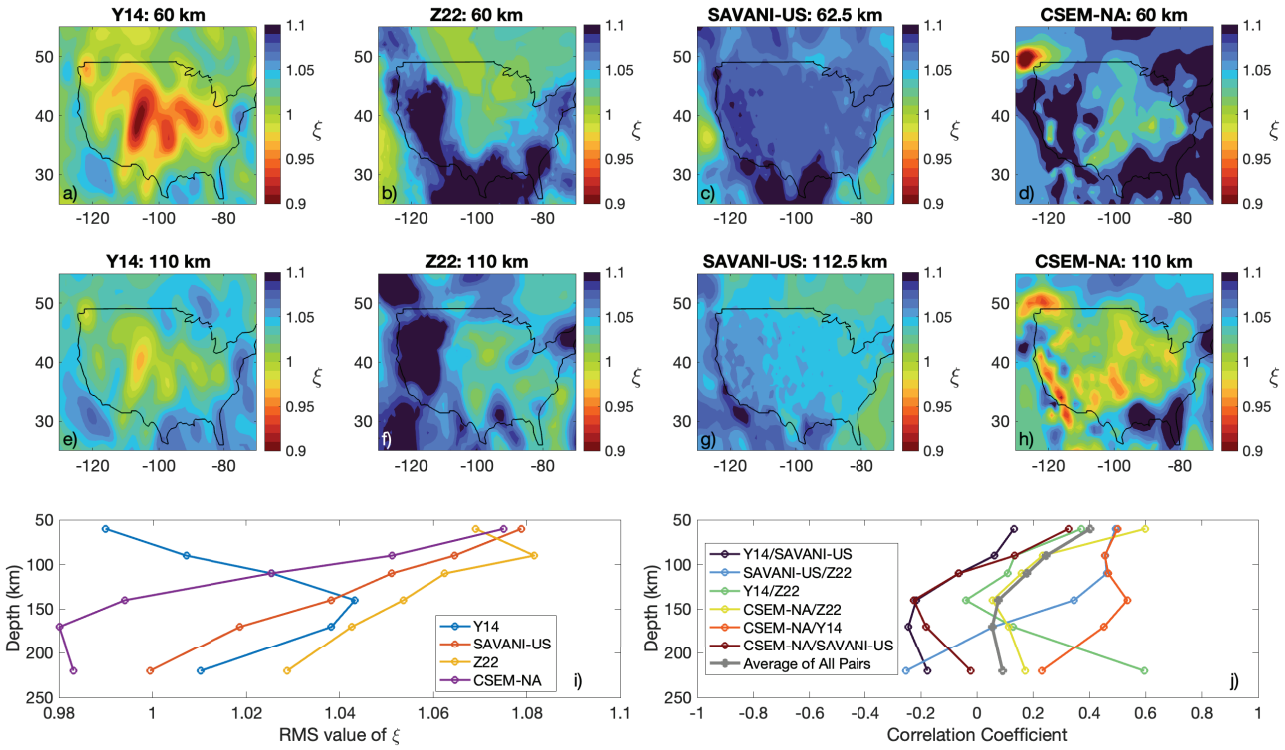

Figure S1. Map view plots of four different models of radial anisotropy ($\xi = (V_{SH}/V_{SV})^2$) at depths of 60 km (a-d) and 110 km (e-h). (i): The average (RMS) strength of radial anisotropy within the conterminous U.S is shown as a function of depth for all models. (j) pair-wise correlation coefficient for all model pairs and the average of all pairs for structure within the conterminous U.S. Calculations (i) and (j) only used structure within the black polygon. The models used are Y14 (Yuan et al., 2014), Z22 (Zhu et al., 2017), SAVANI-US (Porritt et al., 2021), and CSEM-NA (Fichtner et al., 2018).

Figure S2

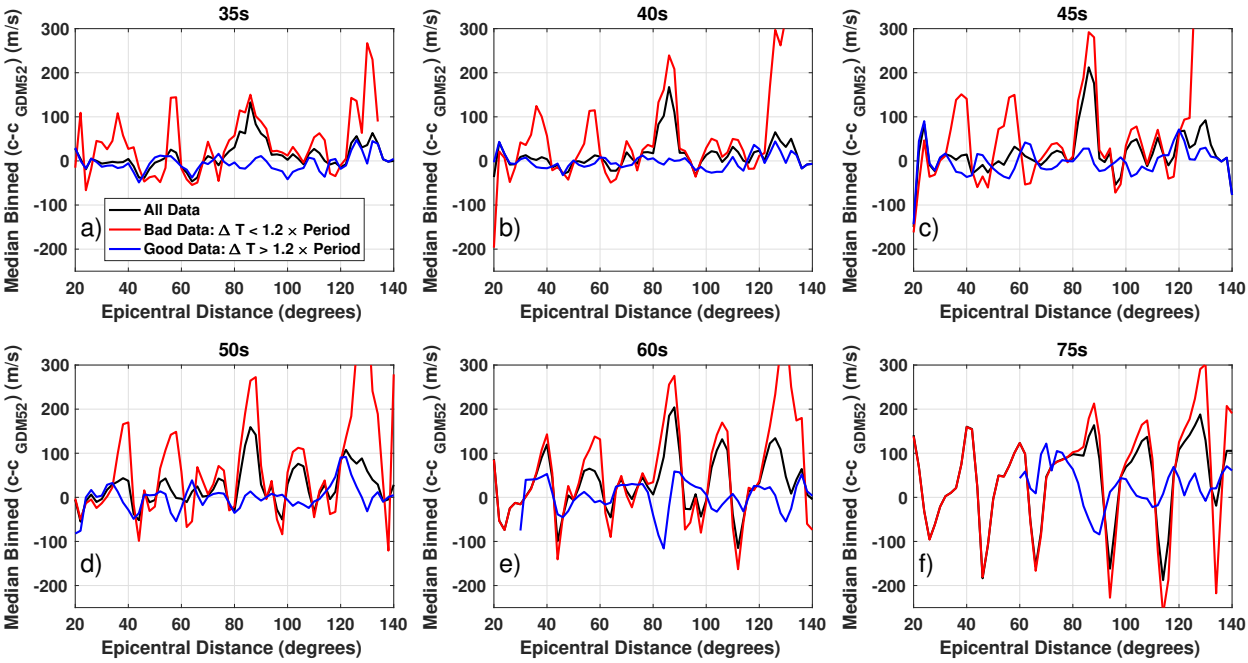

Figure S2. (a-f): Distance dependence of error in phase velocity measurements for different periods, shown in the title. Blue line: Only using data that pass our quality control criteria. Red line: Only data that fail our quality control criteria. Black line: All data.

Figure S3

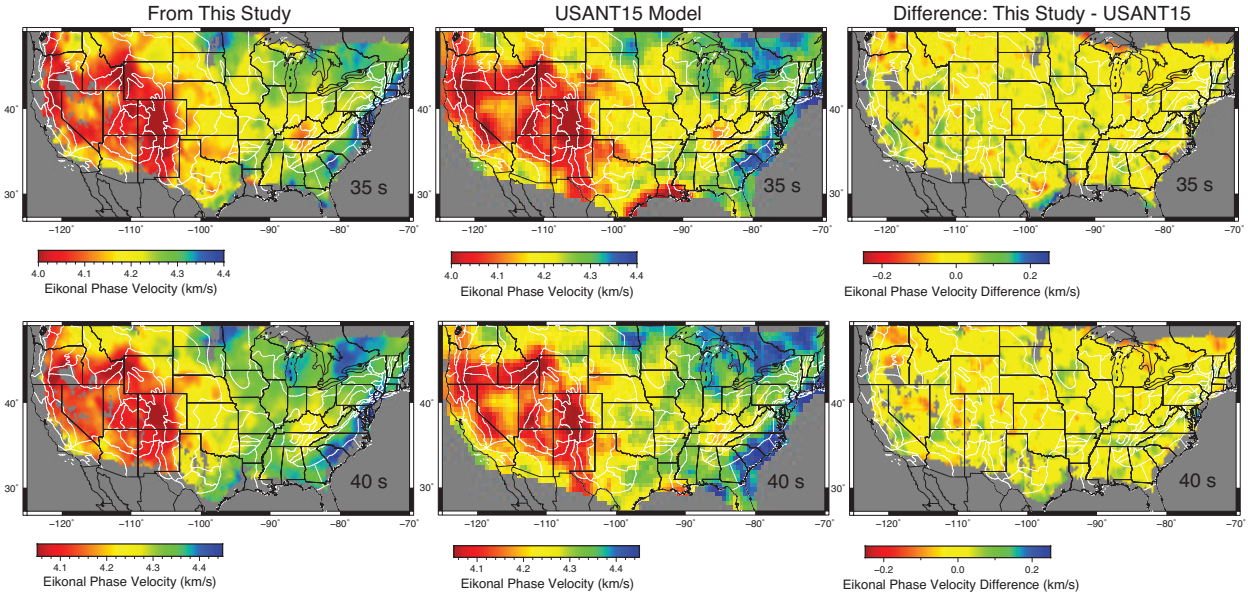

Figure S3. Comparison of earthquake-derived phase velocity maps generated from this study with ambient-noise-derived maps from the USANT15 model (Ekström, 2017). Left column: map view plots of our models. Center: map view plots of the USANT15 model. Right: Difference between both models, with the USANT15 maps subtracted from our maps. Top row: 35 s. Bottom row: 40 s.

Figure S4

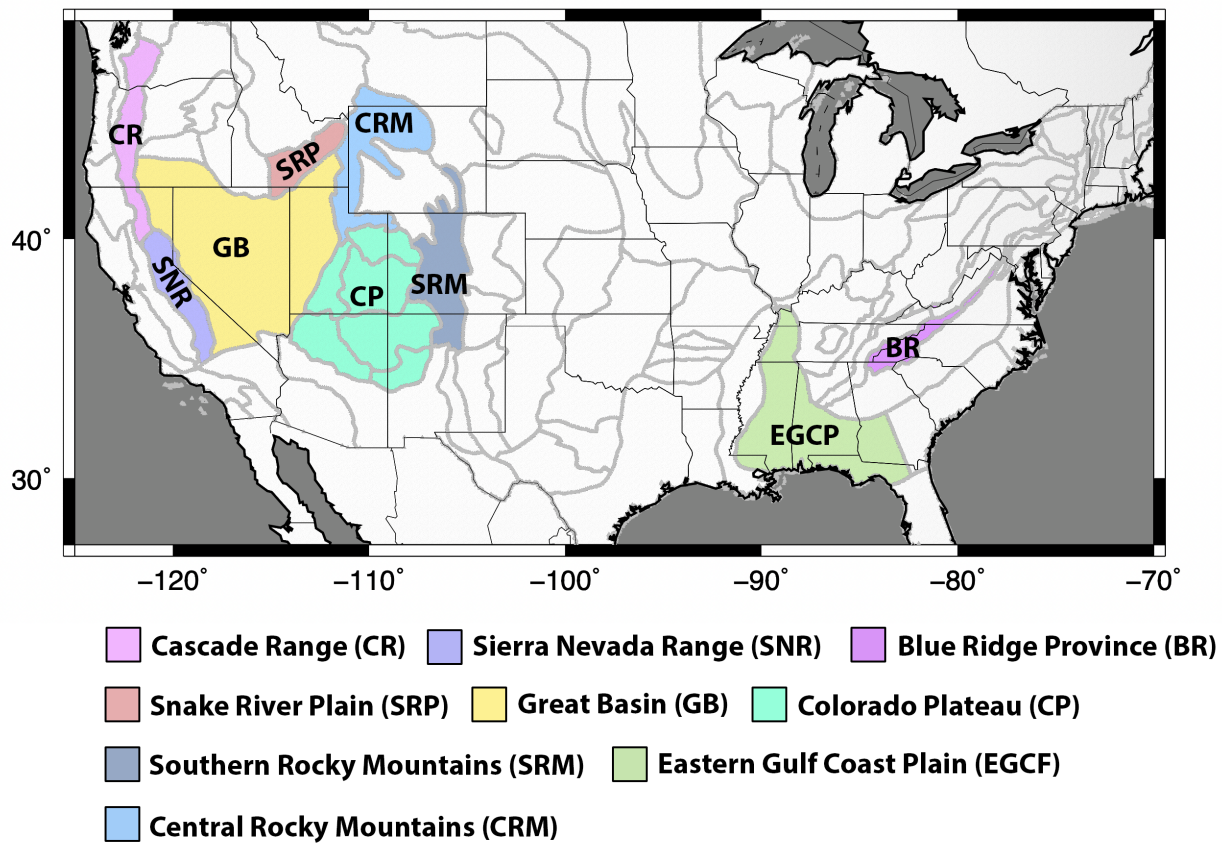

Figure S4. Labeled map of the U.S. showing physiographic features discussed in the main text. Physiographic features (Fenneman, 1928) are plotted as gray lines, with state boundaries overlain in black.

Figure S5

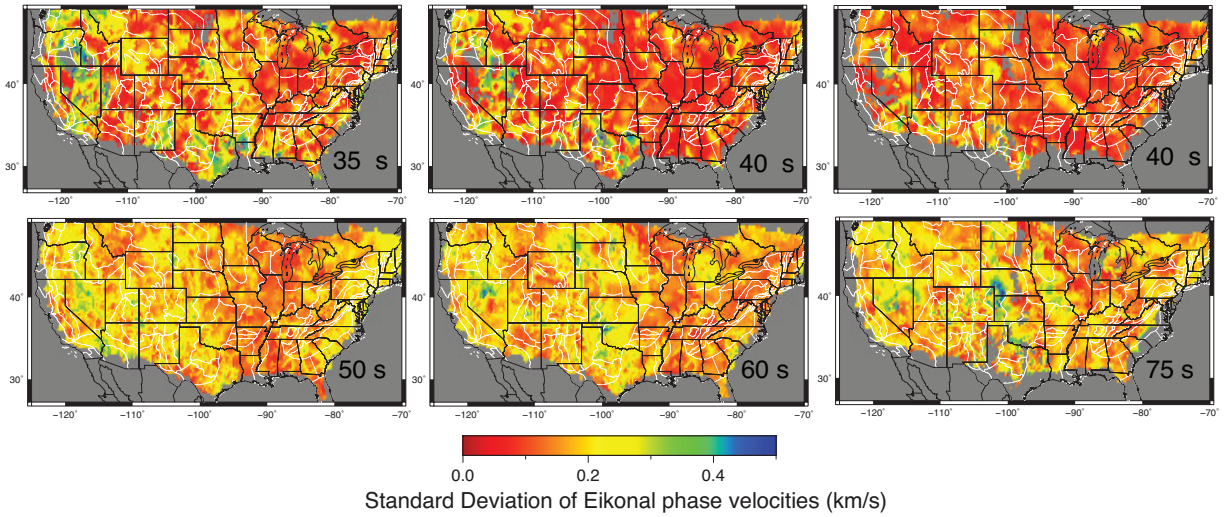

Figure S5. Standard deviation of phase velocity measurements at every pixel after quality control, visualized in map view for all periods in this study. The period corresponding to each map is shown in the bottom-right corner of each map.

Figure S6

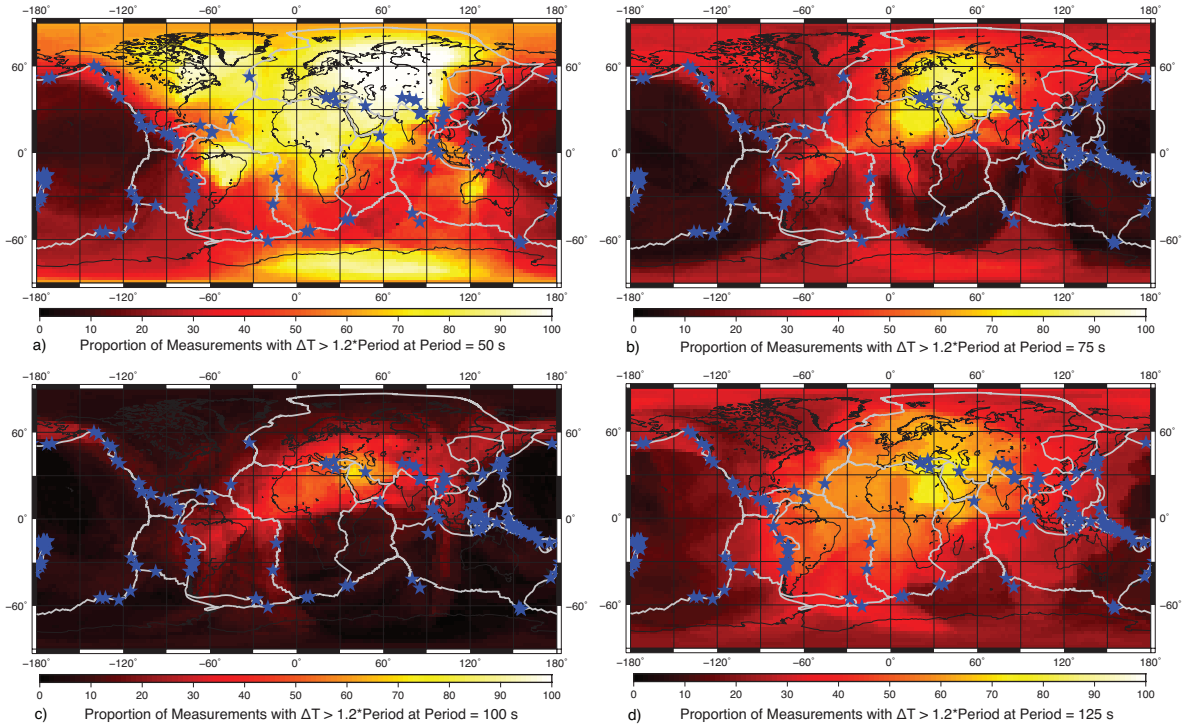

Figure S6. (a-d) Maps showing the fraction of measurements that would satisfy our quality control criteria, assuming every pixel on the Earth's surface records every earthquake from the Global CMT catalog with $M_w \geq 6$ through 2014 and 2015. Earthquakes used in this test are from the Global CMT catalog (Ekström et al., 2012), and their locations are plotted as blue stars. Plate boundaries from Bird (2003) are overlain as gray lines.

References

Babikoff, J. C., & Dalton, C. A. (2019). Long period Rayleigh wave phase velocity tomography using USArray. *Geochemistry, Geophysics, Geosystems*.

Bird, P. (2003). An updated digital model of plate boundaries. *Geochemistry, Geophysics, Geosystems*, *4*(3).

Ekström, G. (2011). A global model of Love and Rayleigh surface wave dispersion and anisotropy, 25-250 s. *Geophysical Journal International*, *187*(3), 1668–1686.

Ekström, G. (2017). Short-period surface-wave phase velocities across the conterminous united states. *Physics of the Earth and Planetary Interiors*, *270*, 168–175.

Ekström, G., Nettles, M., & Dziewoński, A. (2012). The global CMT project 2004–2010: Centroid-moment tensors for 13,017 earthquakes. *Physics of the Earth and Planetary Interiors*, *200*, 1–9.

Fenneman, N. M. (1928). Physiographic divisions of the united states. *Annals of the Association of American Geographers*, *18*(4), 261–353.

Fichtner, A., van Herwaarden, D.-P., Afanasiev, M., Simutė, S., Krischer, L., Çubuk-Sabuncu, Y., ... others (2018). The collaborative seismic earth model: generation 1. *Geophysical research letters*, *45*(9), 4007–4016.

Lin, F.-C., Ritzwoller, M. H., & Snieder, R. (2009). Eikonal tomography: surface wave tomography by phase front tracking across a regional broad-band seismic array. *Geophysical Journal International*, *177*(3), 1091–1110.

Porritt, R. W., Becker, T. W., Boschi, L., & Auer, L. (2021). Multiscale, radially anisotropic shear wave imaging of the mantle underneath the contiguous united states through joint inversion of usarray and global data sets. *Geophysical Journal International*, *226*(3), 1730–

1746.

Yuan, H., French, S., Cupillard, P., & Romanowicz, B. (2014). Lithospheric expression of geological units in central and eastern north america from full waveform tomography. *Earth and Planetary Science Letters*, *402*, 176–186.

Zhu, H., Komatitsch, D., & Tromp, J. (2017). Radial anisotropy of the north american upper mantle based on adjoint tomography with usarray. *Geophysical Journal International*, *211*(1), 349–377.